Journal of Applied Geophysics 87 (2012) 94–106

Contents lists available at SciVerse ScienceDirect

Journal of Applied Geophysics

journal homepage: www.elsevier.com/locate/jappgeo

Quasi-Newton inversion of seismic first arrivals using source finite bandwidth assumption: Application to subsurface characterization of landslides

Julien Gance [a,b,*], Gilles Grandjean [a], Kévin Samyn [a], Jean-Philippe Malet [b]

[a] BRGM, Bureau de Recherches Géologiques et Minières, 3 Avenue Claude Guillemin, F-45060 Orléans, France
[b] Institut de Physique du Globe de Strasbourg, CNRS UMR 7516, EOST/Université de Strasbourg, 5 rue Descartes, 67084 Strasbourg Cedex, France

ARTICLE INFO

Article history:
Received 6 June 2012
Accepted 17 September 2012
Available online 28 September 2012

Keywords:
Inverse theory
Seismic tomography
Fresnel wavepaths
Finite frequency
Resolution improvement
Landslide

ABSTRACT

Characterizing the internal structure of landslides is of first importance to assess the hazard. Many geophysical techniques have been used in the recent years to image these structures, and among them is seismic tomography. The objective of this work is to present a high resolution seismic inversion algorithm of first arrival times that minimizes the use of subjective regularization operators. A Quasi-Newton P-wave tomography inversion algorithm has been developed. It is based on a finite frequency assumption for highly heterogeneous media which considers an objective inversion regularization (based on the wave propagation principle) and uses the entire source frequency spectrum to improve the tomography resolution.
The Fresnel wavepaths calculated for different source frequencies are used to retropropagate the traveltime residuals, assuming that in highly heterogeneous media, the first arrivals are only affected by velocity anomalies present in the first Fresnel zone. The performance of the algorithm is first evaluated on a synthetic dataset, and further applied on a real dataset acquired at the Super-Sauze landslide which is characterized by a complex bedrock geometry, a layering of different materials and important changes in soil porosity (e.g. surface fissures). The seismic P-wave velocity and the wave attenuation are calculated, and the two tomographies are compared to previous studies on the site.

1. Introduction

Near-surface geophysical techniques have a great potential to image subsurface structures in many geomorphological studies (Schrott and Sass, 2008; van Dam, 2010), and even more specifically for improving the knowledge on landslide features (Jongmans and Garambois, 2007). Landslide analysis generally involves the combined use of several geophysical methods to image different petrophysical parameters (Bruno and Marillier, 2000; Mauritsch et al., 2000; Méric, 2006). Seismic surveys are particularly well adapted to detect and characterize changes in compaction and rheology of the material (Grandjean et al., 2007), changes in fissure density at the surface (Grandjean et al., 2012), and complex slip surface geometries (Grandjean et al., 2006). As the wave propagation is mainly controlled by the elastic properties of the medium, seismic surveys are often well correlated with geotechnical observations.

Among them, different approaches can be used for data processing depending on the analysis of different wave types associated with particular propagation phenomena. Bichler et al. (2004) and Bruno and Marillier (2000) interpreted the late arrivals of P-waves to image the bedrock geometry using seismic reflection analysis. Mauritsch et al. (2000) and Glade et al. (2005) analyzed refracted waves to define the internal geometry (e.g. layering) of landslides. Grandjean et al. (2007, 2011) and Travelletti et al. (in press) studied the first arrival traveltimes to recover P-wave velocity distribution. More recently, Samyn et al. (2012) used a 3D seismic refraction traveltime tomography to provide a seismic and geometrical model of a complex landslide structure. Grandjean et al. (2007, 2011) also used Spectral Analysis of Surface Wave (SASW) techniques to obtain S-wave velocity distributions along landslide cross-sections. Finally, based on the work of Pratt (1999) and Virieux and Operto (2009), Romdhane et al. (2011) demonstrated the possibility to exploit the entire wave signal by performing a Full elastic Waveform Inversion (FWI) on a dataset acquired on a clayey landslide.

These methods are appropriate to image specific geological medium and their relevance depends on the petrophysical properties of the material and the complexity of the layering.

Seismic refraction can be performed using the General Reciprocal Method (GRM; Palmer and Burke-Kenneth, 1980) or the Plus/Minus Method (Hagedoorn, 1959). These methods are relatively fast and easy to implement, but based on simple hypotheses (such as a layered media) and are consequently not very efficient to recover important variations in lateral seismic velocity. Seismic reflection surveys need to record high frequency signals to obtain a good resolution of final stacked sections; they are difficult to set up for subsurface applications

* Corresponding author at: BRGM, Natural Hazard Department, 3 Avenue Claude Guillemin, BP 36009, 45060 Orléans Cedex 2, France. Tel.: +33 2 38 64 38 19; fax: +33 2 38 64 35 49.
E-mail address: j.gance@brgm.fr (J. Gance).

0926-9851/$ – see front matter © 2012 Elsevier B.V. All rights reserved.
http://dx.doi.org/10.1016/j.jappgeo.2012.09.008

because of the strong attenuation affecting high frequencies and decreasing the signal to noise ratio (Jongmans and Garambois, 2007). Moreover, these methods produce a reflection image more adapted to describe geological structures than to differentiate geotechnical units. FWI appears to be the more advanced method since it can be based on the realistic assumption of an elastic media and uses the whole seismic signal in the inversion scheme. However, it is a complex method requiring an important data pre-processing (source inversion, amplitude correction) that is hardly applicable on a real near surface dataset (complex topography, low signal to noise ratio; Romdhane et al., 2011). As a consequence, recovering the structural image of a landslide from the seismic velocity field estimated with an accurate method is still a challenge.

The objective of this work is to refine the first arrival tomography approach applied to landslide analysis, which is a good compromise between the strong assumptions made in simple refraction methods and the complexity of the FWI technique when used in very heterogeneous soils. P-wave tomography is largely used, from crustal to shallow case studies and allows recovering, at a relatively low cost, a reliable image of the seismic velocity distribution. In this perspective, Taillandier et al. (2009) proposed to develop the first arrival traveltime tomography using the adjoint-state method, but had to face the problem of gradient regularization. The method proposed here is based on a Hessian formulation (Tarantola, 1987) to ensure an optimum convergence of the algorithm during iterations. We only use the first arrivals of the seismic signal corresponding to direct or refracted waves. In that case, late arrivals, including scattering, conversion effects are not taken into account in the inversion.

In the next section, the theory used to formulate the inversion problem and the related approximations introduced in the processing technique are detailed. The final algorithm is tested on a synthetic case in order to estimate the quality of the velocity field reconstruction without considering noisy data. To compare our results with a reference case, the synthetic velocity model is identical to the one used by Romdhane et al. (2011). Then, a real seismic dataset obtained from a seismic survey at the Super-Sauze landslide (South French Alps) developed in clayey material is presented. On this case study, the P-wave velocity and the attenuation fields are inverted. The effects of noisy data on the quality of the reconstructed velocity field are analyzed. The observed surface variation in the velocity and attenuation fields is discussed by integrating other sources of information (geotechnical tests, geomorphological observations).

2. Theoretical approach

2.1. General inverse problem

Solving the inverse problem requires a modeling step (i.e. the forward problem) for computing the residuals (i.e. the difference between computed and observed data). An updated model can be estimated by back-projecting the data residuals on each cell of the model discrete grid. The forward problem thus consists of finding a relation between the data t, taken here as the first arrival traveltimes and the physical P-wave velocity model s, such as:

$$t = f(s). \tag{1}$$

This problem is generally solved using the asymptotic high frequency wave propagation assumption in a non-homogeneous isotropic medium. The wave propagation equation is then simplified into the eikonal equation that computes the first arrival traveltimes over a discrete grid, for example by using a finite-difference scheme (Vidale, 1988). This technique has been improved for sharp velocity contrasts (Podvin and Lecompte, 1991), optimized by Popovici and Sethian (1998) who proposed the Fast Marching Method (FMM) and by Zhao (2005) who proposed the Fast Sweeping Method recently adapted to non-uniform grids (Sun et al., 2011). The technique is actually largely used because of its efficiency and accuracy.

In this study, the FMM algorithm (Popovici and Sethian, 1998) is used to compute the forward problem. The computation of the first arrival traveltime is generally followed by a ray tracing that uses the traveltime maps to propagate the wavepath from the sources to the receivers. The traveltime t can be expressed using the following matrix form:

$$t = Ls \tag{2}$$

where L is the length of the ray segment crossing each cell of the slowness model s. Generally, the Fermat principle allows the Fréchet derivative matrix to be approximated by the matrix L (Baina, 1998). This principle establishes that a small perturbation δs on the initial model does not change the ray paths, and therefore only affects the traveltime δt at the second order. This linearization of the problem around the slowness model s^k permits to use the Quasi-Newton (Q-N) method and the nonlinear problem can be resumed to a tomographic linear system:

$$\left[\left(L^k\right)^T L^k\right]\delta s^k = \left[\left(L^k\right)^T \delta t\right] \tag{3}$$

where k and T represent respectively the iteration index and the transpose operator. Several techniques can be used to solve Eq. (3). The Simultaneous Iterative Reconstruction Technique (SIRT) is the most commonly used because it does not require a large computer memory; consequently, SIRT is used to invert large sparse linear systems (Trampert and Lévèque, 1990). Its convergence towards a least-square solution has been proved (Van der Sluis and Van der Vorst, 1987) but this method suffers from a few drawbacks: SIRT introduces an intrinsic renormalization of the tomographic linear system that modifies slightly the final solution. For that reason, the LSQR (Least-Square QR) algorithm (Paige and Saunders, 1982) based on an iterative least-squares method using the QR decomposition is preferred in our approach. It has been proved to be superior to SIRT or to Algebraic Reconstruction Techniques (ART) in terms of numerical stability and convergence rates (Nolet, 1985).

2.2. From rays to Fresnel volumes

Revisiting seismic traveltime tomography also needs to consider the ray approximation, i.e. the infinite spectral bandwidth assumption. The main issue of this approximation lies in the traveltime computation taken as line integrals along the rays spreading over the slowness model. Because the slowness values are only considered along ray paths, the problem is often underdetermined and leads to numerical instability (Baina, 1998). In practice, this difficulty is generally by-passed using regularization operators to reduce the non-constrained part of the model, and then, to reinforce the numerical stability. Generally, a simple smoothing of the reconstructed slowness model (Zelt and Barton, 1998), the application of a low-pass filter on the gradient (Taillandier et al., 2009), or the elimination of the lowest eigenvalues in the Hessian matrix (Tarantola, 1987) can be used. However, such regularization operators require the selection of appropriate parameters (filter length, eigenvalue cut-off and more generally the size and weights of the smoothing operators). Kissling et al. (2001) demonstrated the dependency of these parameters on the resolution and the quality of the final model in poor wavepath coverage areas. This is the reason why the use of physically-based regularization operators such as Fresnel volumes or sensitivity kernels is preferable since they are based on non-subjective principles completely defined by the problem.

With this assumption, several methods have been developed including those using the concept of Fresnel volumes as a regularization factor. Nolet (1987) proposed to use the size of the Fresnel zone to

constrain the size of a spatial smoothing operator. Vasco et al. (1995), Watanabe et al. (1999); Ceverny (2001) and Grandjean and Sage (2004) used the Fresnel volume in the back projection of the residuals.

More recently, the concept of sensitivity kernels or Fréchet Kernel introduced by Tarantola (1987) has been reformulated for traveltime tomography. It represents a good compromise between the strong assumption of the asymptotic ray theory and the high computational cost of the complete full wave inversion tomography (Liu et al., 2009). While the ray theory is well adapted in media characterized by geological structures larger than the first Fresnel zone, the use of sensitivity kernels allows to overcome this constraint and thus, to increase the spatial resolution (Spetzler and Snieder, 2004). Several authors have developed this concept and investigated the properties of the sensitivity kernels for traveltime tomography in homogeneous media, mainly at the spatial scale of the earth crust (Dahlen, 2005; Dahlen et al., 2000; Zhao and Jordan, 2006). The strategies proposed by these authors are generally limited to smoothly heterogeneous media (Liu et al., 2009; Spetzler et al., 2008) and are barely applied to real datasets, mainly because of prohibitive calculation costs (Liu et al., 2009).

Sensitivity kernels and Fresnel volumes are based on the single scattering (Born) approximation. With this approximation, seismic velocity anomalies in the vicinity of the ray path can reduce the first arrival time of a part of the wave. For highly heterogeneous media, this approximation is not valid anymore because multiple scattering should be taken into account to fully explain observed first arrivals.

In this context, an accurate computation of the sensitivity kernel is useless. That's why we choose to use a simplified sensitivity kernel defined empirically only in the first Fresnel zone. This approximation can be justified by the fact that first Fresnel zone is the region of highest sensitivity (Liu et al., 2009). This simplified sensitivity kernel will be constructed as a weighted Fresnel wavepath used by Grandjean and Sage (2004). It will permit nevertheless to take into account the possible change in first arrival traveltimes due to velocity anomalies in the vicinity of the ray path and to address issues of regularization by using increasing finite frequency bandwidths.

In the next section, the Fresnel volumes, defined as a simplification of the sensitivity kernels, and their implementation in a Q-N algorithm are presented.

First, the Fresnel weights proposed by Watanabe et al. (1999) and used by Grandjean and Sage (2004) in order to materialize the wavepath in the model are expressed. They classically decrease linearly from a value of one (when the cell is positioned on the ray path) to a value of zero (when the cell is out of the Fresnel volume):

$$\omega = \begin{cases} 1-2f\Delta t, & 0 \le \Delta t < \dfrac{1}{2f} \\ 0, & \dfrac{1}{2f} \le \Delta t \end{cases}. \tag{4}$$

Watanabe et al. (1999) and Grandjean and Sage (2004) defined these weights ω as the probability that a slowness perturbation delays the arrival of the wave by a Δt considering that f is the considered frequency of the wave. This definition is interesting because of its simple expression that allows fast computing while taking into account the global shape of the 2D traveltime sensitivity kernel given in Spetzler and Snieder (2004) and corresponding to a decrease of sensitivity until the first Fresnel zone. Because the size of the Fresnel volume is depending on the considered source frequency, a new inversion strategy based on increasing frequencies can be proposed. To consider the entire source frequency content, some authors compute wavepaths in a band-limited sensitivity kernel, stacking the monochromatic kernels with a weight function similar to the amplitude spectrum of the wavelet (Liu et al., 2009; Spetzler and Snieder, 2004). In our approach, the Fresnel weights are computed for a monochromatic wave, increasing its frequency at each iteration of the inversion. The considered frequency is sampled with an increasing rule ranging from the lower to the higher frequency of the source signal. The same weight is assigned to all frequencies in order to limit the number of iteration and to preserve the rapid convergence of the algorithm. Taillandier et al. (2009) showed that this method applied to the gradient filtering permits to mitigate the non-linearity of the problem. For low frequency values, the Fresnel zone will be larger and the slowness model will be reconstructed with large wavelengths. Conversely, for high frequency values, the Fresnel zone will be thinner and the slowness model will be reconstructed with sharp wavelengths. This strategy, already used in FWI revealed to be efficient to progressively reconstruct the small features of the inverted model and prevent convergence toward a local minimum caused by cycle skipping issues (Romdhane et al., 2011; Sirgue and Pratt, 2004; Virieux and Operto, 2009). Recovering slowness variations which sizes are in agreement with each wavelength transmitted by the source should lead to better images of local heterogeneities while preserving the algorithm convergence.

With these assumptions, the traveltime perturbation can be expressed as the integral over a Fresnel volume multiplied by the slowness perturbation field observed for all points r in the volume (Liu et al., 2009). This linear relationship among traveltime and slowness perturbation is the result of the first Born approximation that is only valid for a small perturbation (Yomogida, 1992):

$$\delta t = \int W(r)\delta s(r)dr \tag{5}$$

where W is the Fresnel weight operator (Fig. 1) normalized by the area of the Fresnel ellipse perpendicular to the ray path a, for each shot and receiver such as:

$$W(r) = \frac{1}{a}\omega(r). \tag{6}$$

This normalization allows linking our approach to the geometrical ray theory in the case of a plane wave propagation (Liu et al., 2009; Spetzler and Snieder, 2004; Vasco et al., 1995), so that the integral of W over a surface perpendicular to the wavepath is equal to one, which is generally verified for sensitivity kernels:

$$\int_{-\infty}^{+\infty} W(s,r,f)ds = 1. \tag{7}$$

The defined Fresnel volume, also called Fréchet kernel, corresponds to the Fréchet derivative (Tarantola, 1987; Yomogida, 1992) or Jacobian matrix of the forward problem, similar to the length of ray segment matrix L defined in the asymptotic ray theory. The problem, considered in 2D, can then be written in its matrix form (Vasco et al., 1995):

$$\delta t = W\,\delta s \tag{8}$$

where W is the [*number of data* × *number of cells*] Fresnel weight matrix, calculated for each shot and for each receiver such as for the cell j and for the couple source-receiver i:

$$W_{ij} = \frac{\omega_{ij}}{l} \tag{9}$$

where l is the length of the Fresnel surface along a direction perpendicular to the ray path.

However, the readers have to be aware that the use of the Fresnel weight as defined previously is a rough approximation of the wavepath. This is the reason why the ray assumption is kept to compute traveltimes, avoiding the introduction of any error due to this approximation. This choice has been justified by Liu et al. (2009) who observed small differences between traveltime values computed with both approaches.

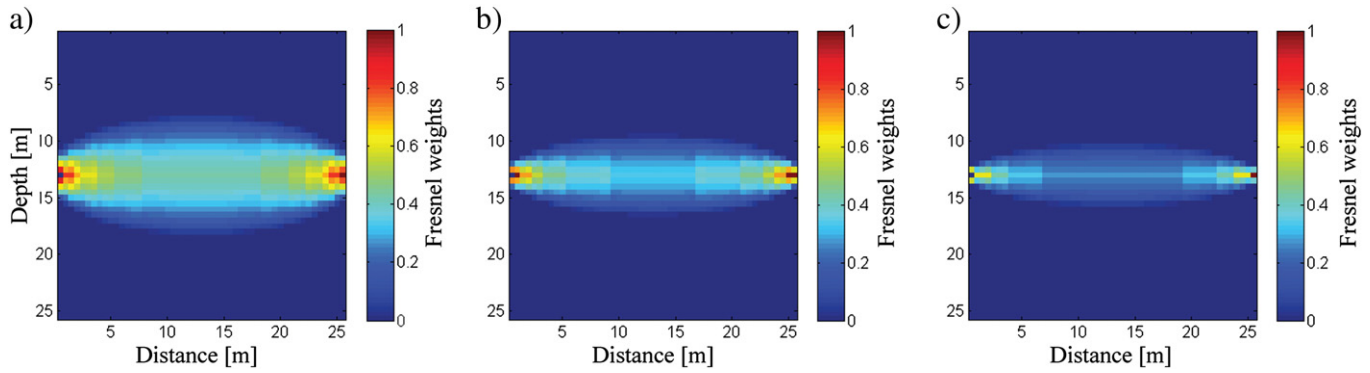

Fig. 1. Fresnel weights (e.g. distance versus depth) computed for a medium characterized by a constant velocity of 500 m.s^{-1} and for three frequencies: a) 100 Hz, b) 200 Hz and c) 300 Hz. The source is located at x = 0 m and the receptor at x = 25 m, both at 12.5 m of depth.

2.3. New implementation of the inverse problem

In the previous section, the combination of the Born approximation with Fresnel volumes allowed the estimation of the Fréchet derivative. To solve the nonlinear inverse problem, a steepest descent iterative algorithm is used to minimize the L_2 norm misfit function l (Tarantola, 1987) that can be written in this particular case:

$$l(s) = \frac{1}{2}\left[(f(s)-t_{obs})^T C_T^{-1}(f(s)-t_{obs}) + \left(s-s_{prior}\right)^T C_S^{-1}\left(s-s_{prior}\right)\right] \quad (10)$$

where C_T and C_S are respectively the covariance operators on data and model, f represents the theoretical relationship between the model s and the traveltimes t, t_{obs} the observed data and s_{prior} the a priori information on the model.

The Q-N method consists of minimizing the misfit function iteratively using its gradient and approximated Hessian matrix. The gradient gives the direction of steepest descent of the misfit function while the Hessian matrix is used as a metric indicating its curvature, approximated locally by a paraboloid (Tarantola, 1987). Compared to the gradient method, the Hessian is here used to improve the assessment of direction and norm of the updated vector that is applied to the slowness model, so that each iteration is performed in the good direction and with an optimized length. The tomographic linear system in the case of no a priori information on the model can be written in its matrix form:

$$\left[\left(W^k\right)^T C_T^{-1}\left(W^k\right)\right]\delta s = \left[\left(W^k\right)^T \delta t\right]. \quad (11)$$

This linear tomographic system is solved by using a LSQR algorithm. The Fresnel weight matrix is a [*number of data* × *number of cells*] matrix. Its computation is straightforward on classical personal computers. The Q-N algorithm is based on the inverse of the Hessian matrix that is a square matrix of size [*number of data* × *number of data*] that can be difficult to invert for large datasets. Iterative solutions are generally used to approximate the inverse Hessian matrix from successive gradient vectors to save time and memory (e.g. BFGS). In our approach, the approximate Hessian matrix is computed from the Fresnel weight matrix to fully use the contribution of the Fresnel wavepaths. This solution is more time consuming and requires cluster computing to invert our data. The step size is optimized along the direction given by the product of the gradient and of the inverse Hessian using a scalar to weight the slowness update with a parabolic interpolation (Tarantola, 1987).

2.4. Validation on a synthetic dataset

The algorithm is tested on the synthetic transverse section used by Romdhane et al. (2011) representing a typical cross-section of a landslide body overlying a homogeneous bedrock (Fig. 2a). The performance of the method is discussed by taking as a reference the SIRT algorithm of Grandjean and Sage (2004).

The synthetic dataset, calculated with a simple 2D eikonal equation solver, is composed of 50 shots recorded on 100 geophones. The model consists of 209 × 68 cells of 1 m in width. The seismic sources are spaced regularly every 2 m and the geophones every 1 m. The synthetic model is composed of ten layers with P-wave velocity ranging from 330 m.s^{-1} to 3300 m.s^{-1}. Except for the zone between the landslide body and the bedrock, the changes in P-wave velocity are small, so that it is difficult to reconstruct the detailed shape of the landslide body. The initial model is a simple constant velocity gradient model, with velocities ranging from 330 m.s^{-1} to 3300 m.s^{-1}. The stopping criterion is a change in the cost function lower than 1% and the inversion is limited to 20 iterations. For both algorithms, we performed the inversion with a 30 Hz frequency. For the Q-N algorithm, the frequency increases linearly at each iteration, until the sixth one to 120 Hz. Fig. 2b and c shows the results obtained with the SIRT (Grandjean and Sage, 2004) and the Q-N algorithms. They converge respectively after 15 and 20 iterations. The convergence of the misfit function is better for the Q-N algorithm with a value 3.6 times lower than the SIRT. Globally, the Q-N algorithm succeeds in recovering the shape of a bump at 2000 m.s^{-1} located on the left side of the cross-section and renders a more spatially detailed shape of the bedrock geometry (Fig. 2b, c). The SIRT algorithm does not retrieve those initial structures. However, both algorithms have difficulties to reproduce the low velocity of the very near surface layer, because of the poor ray coverage in this area.

Fig. 2d, e and f compares the results on three vertical sections chosen to highlight the ability of the Q-N algorithm to recover P-wave velocity with a better accuracy than the SIRT. We can notice that for the top-soil, P-wave velocities are the same for both algorithms and are equal to the P-wave velocities of the initial model in that zone. The Q-N algorithm is able to recover smaller wavelengths than the SIRT. As shown in Fig. 2d, between 55 and 60 m of depth, the vertical profile corresponding to the Q-N algorithm shows sudden variations in depth that appear smoothed on the SIRT.

This synthetic example demonstrates the ability of the Q-N algorithm to recover the shape of the internal layers. Contrary to the SIRT, the Q-N allows to better interpret the thickness and geometry of these layers.

3. Application of the Q-N algorithm on a real dataset

3.1. Geomorphological characteristics of the study site

The Q-N algorithm has been applied on a real dataset acquired at the Super-Sauze landslide (South French Alps), developed in Callovo–Oxfordian black marls. Its elevation is between 2105 m at

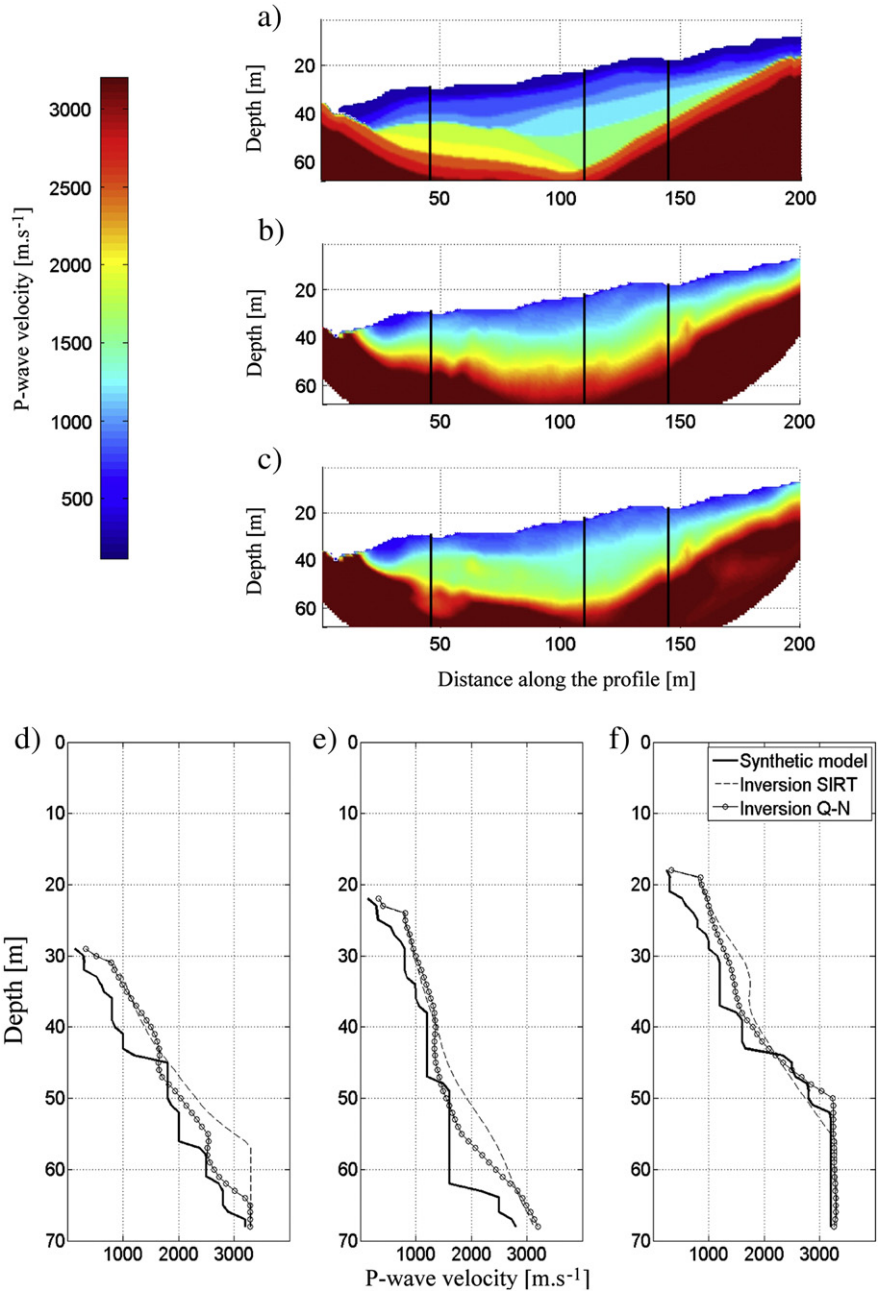

Fig. 2. Algorithm validation on a synthetic dataset: a) synthetic initial model, b) final velocity model inverted with the SIRT algorithm, and c) final velocity model inverted with the Q-N algorithm. Vertical cross-sections extracted from the three models at a distance of d) 46 m, e) 110 m and f) 145 m.

the crown and 1740 m at the toe. The landslide is continuously active with displacement rates of 0.05 to 0.20 m.day^{-1} on average (Malet et al., 2005a). The detachment of large blocks of marls from the main scarp (Fig. 3d) and their progressive mechanical and chemical weathering in fine particles explain the strong grain size variability of the material especially in the topsoil (e.g. decametric blocks of marls at various stages of weathering, decimetric and centimetric clasts of marls, silty-clayey matrix; Maquaire et al., 2003). The bedrock geometry is complex with the presence, in depth, of a series of in-situ black marl gullies, partially or totally filled with the landslide material (Flageollet et al., 2000; Travelletti and Malet, 2012). This complex geometry delimits compartments of different hydrogeological, rheological and kinematical characteristics. The variable displacement rates and the bedrock geometry control the presence of dense fissure networks at the surface (Fig. 3b, c) that can be imaged with joint electrical and electromagnetic methods (Schmutz et al., 2000). Many kinds of heterogeneities are observed at different scales, and they control directly the mechanical behavior of the landslide by creating excess pore water pressures (Travelletti and Malet, 2012; Van Asch et al., 2006). The top soil surface characteristics have a large influence on the surface hydraulic conductivity (Malet et al., 2003) and therefore, on the rate of water infiltration (Debieche et al., 2009; Malet et al., 2005b). In this context, we tested the Q-N P-wave tomography inversion scheme to provide a high-resolution characterization of structures and to detect small scale heterogeneities along a N–S transect of the landslide.

3.2. P-wave velocities inversion

The seismic profile is parallel to the sliding direction of the mass and is located in the upper part from a secondary scarp to the middle

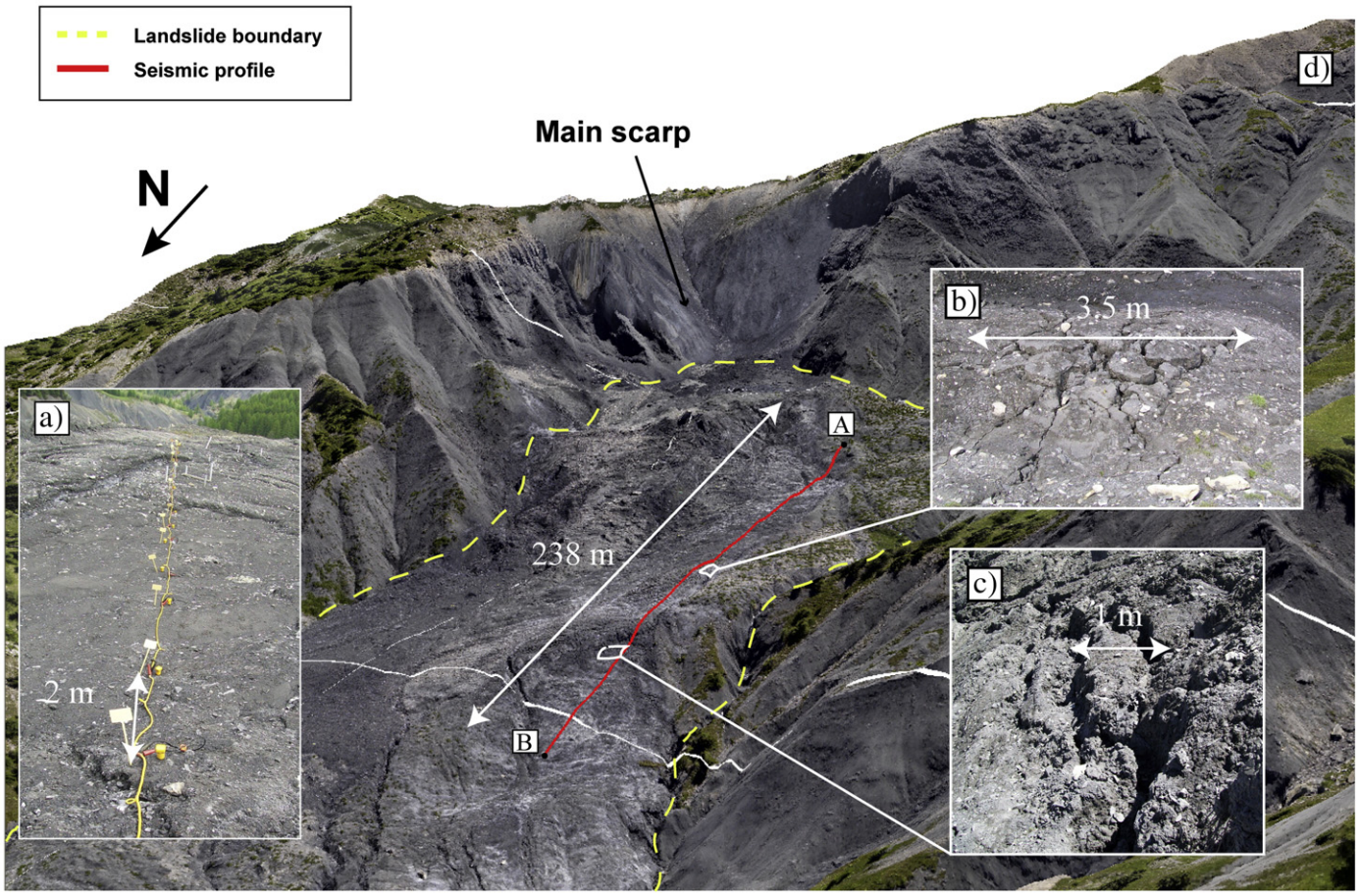

Fig. 3. Location of the investigated area within the Super-Sauze landslide. The seismic profile (red) is represented on an orthophotograph overlaid on a digital elevation model of the landslide. The main scarp and the landslide limit. Picture a) shows the seismic device on the field. Pictures b) and c) represent the observed fissure state of the soil along the profile.

part of the accumulation zone (Fig. 3a and d). The base seismic device had a length of 94 m and consisted of 48vertical geophones (with a central frequency of 10 Hz) regularly spaced every 2 m. Sixty shots have been achieved with a hammer every 4 m. A roll-along procedure has been used to translate the acquisition cables with a 24 geophone overlap in order to investigate a 238 m long profile. The recording length is 1.5 s with a sample rate of 0.25 ms and the acquisition system consists of a Geometrics Stratavisor seismic camera (48 channels). All shots have a relatively good signal to noise ratio until the last geophone in the upper part of the section (Fig. 4b). The shots acquired in the lower part are affected by the higher density of fissures. The attenuation and the signal to noise ratio are consequently higher in this part of the profile. The signal is dominated by the surface waves but the first arrivals are clearly visible for all shots.

To estimate the picking uncertainty, the time differences of the picks from reciprocal source–receiver pairs was examined. Two people picked the first arrivals of the waves, and the differences between reciprocal traveltimes were studied for each created dataset. Three subsets were created: the first subset was kept intact; in the second subset, picks having more than 10 ms of difference in traveltimes reciprocity were corrected, and in the third subset, picks having more than 10 ms of difference in traveltimes reciprocity were removed. All datasets were inverted and the one which gave the lower final misfit function value and the most reliable P-wave tomogram with

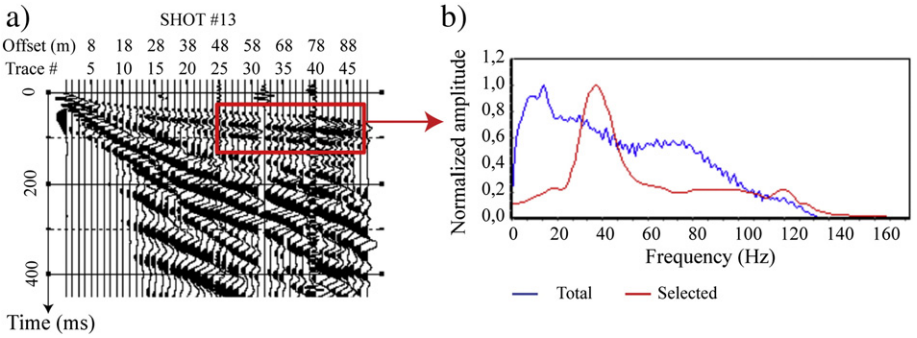

Fig. 4. Data quality: a) seismic shot# 13. b) Source amplitude spectrum of the total seismic shot (blue) and source amplitude spectrum of the P-wave of the selected area (red). (For interpretation of the references to color in this figure legend, the reader is referred to the web version of this article.)

our a priori knowledge of the study site was kept. The differences between the P-wave tomograms were not important, but the selected dataset permitted to interpret the results unequivocally. The error in traveltimes reciprocity distribution is approximated by a Gaussian belt with a standard deviation of 2.2 ms (Fig. 5).

The inversion has been performed with the Q-N algorithm on a 358×153 regular grid composed of square cells of 0.67 m. The hammer source gave frequencies comprised between 30 Hz and 120 Hz with a dominant frequency of 40 Hz. Those frequencies are also present in the P-wave up to the end of the profile (Fig. 4b). Regarding the different amplitude spectra, these values are considered as constant for each shot. For the first iteration, the frequency was set to 30 Hz and then increased at each iteration to respectively 45 Hz, 60 Hz, 75 Hz, 90 Hz, 105 Hz and 120 Hz; after the eighth iteration, the frequency was kept constant at 120 Hz. Thus, the initial width of the Fresnel zone is progressively divided by 1.5, 2, 2.5, 3, 3.5 and 4 in a homogeneous media.

The initial model is of high importance for a good convergence as the linearization of the problem around the initial model is only valid for a model close to the real one. This reason motivates the automated calculation of the initial model from the data using a simplified slant-stack algorithm transforming the dataset in the velocity-intercept time domain. Theoretical traveltime curves were calculated in a double loop for a velocity v ranging from v_{min} to v_{max} (defined by the user) and for a range of intercepts τ such as:

$$t = \tau + \frac{offset}{v}. \tag{12}$$

For each of these theoretical curves, the model was compared to the observed traveltimes; the points with a difference of less than 0.5 ms were stored in the τ-p plan (Fig. 6a). For each intercept, the velocity corresponding to the maximum number of points was used to create a profile of velocity that is further used under the shot point (Fig. 6b).

The depth d corresponding to each velocity was then deduced from the velocities by using Eq. (13):

$$d(i) = d(i-1) + v(i) * \delta t \tag{13}$$

where δt represents the sample rate of intercepts (Fig. 6c).

The velocity profiles were gathered to construct the initial model that was finally smoothed to avoid lateral artifacts. With a misfit function value of 0.3612, this initial model is supposed to be as much as possible close to the final one, in order to avoid divergence or convergence in local minima. The stopping criteria were set to a percentage change lower than 1% and the maximum number of iteration was limited to 20. The misfit function value associated to the final model is 0.0122 and has been obtained after 17 iterations. The inversion has been performed on a multicore computer with 32 GB memory and lasted 1.3 day. Fig. 7 shows the misfit functions related to the SIRT and Q-N algorithms.

Fig. 8 shows respectively the initial velocity model and the inverse models obtained with the SIRT and Q-N algorithms. The upper part of the profile (between the abscissa 0 and 100 m) presents a smoother contrast between the landslide mass and the bedrock for the SIRT result (Fig. 8b and c). Although two bumps are visible at the abscissa 100 and 140 m, the depression located in between is not visible. In the lower part of the profile, the active layer obtained with the SIRT algorithm is deeper than for the Q-N algorithm and presents only few lateral heterogeneity. Globally, the SIRT and Q-N tomographies are in agreement, but the SIRT algorithm does not permit to recover the geotechnical unit limits with the same accuracy.

3.3. Seismic wave attenuation tomography

The amplitude of the first arrival is exploited to image the wave attenuation. Seismic wave attenuation is an efficient physical property because it can be directly linked to porosity and to the presence of fissures in the media (Schön, 1976). Several attenuation parameters can be used to invert seismic attenuation (spectral ratio, centroid frequency shift and peak frequency shift; De Castro Nunes et al., 2011). The simple method proposed by Watanabe and Sassa (1996) is used in our approach; it considers that in a homogeneous attenuation medium, the amplitude of the spherical wave verifies:

$$A(r) = \frac{A_0}{r} e^{-\alpha r} \tag{14}$$

where A_0 is the amplitude of the source signal, r the distance from the seismic source along the ray path and α the attenuation coefficient.

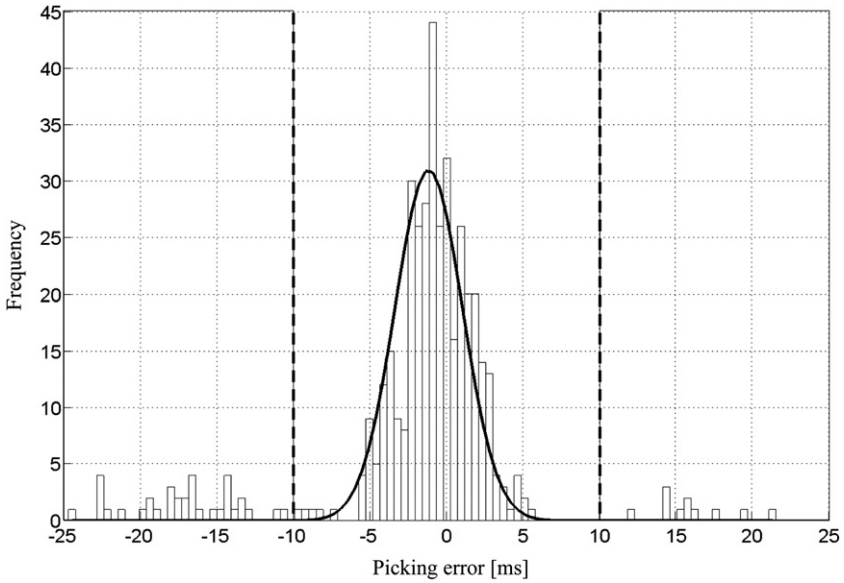

Fig. 5. Picking quality: frequency distribution of differential traveltime errors (e.g. due to reciprocal differences). The standard deviation has a value of 2.2047 ms for 427 tested reciprocal traveltimes. The gray color indicates the data rejected in the inversion process.

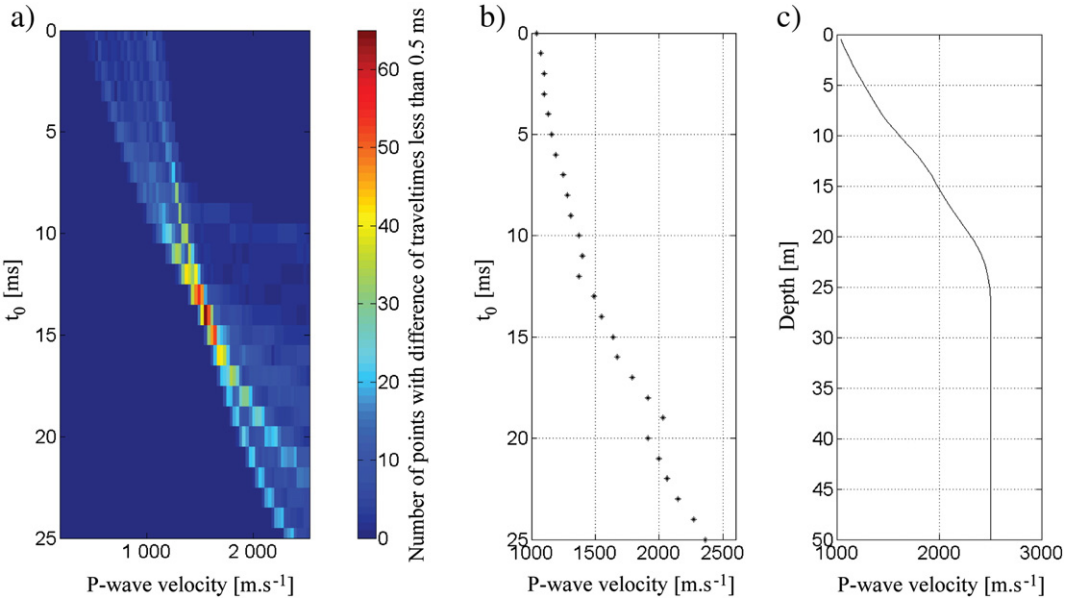

Fig. 6. Example of vertical P-wave velocity profile for the seismic shot #4: a) slant-stack transformation in the t–v (time–velocity) domain for the seismic shot #4, b) estimated vertical velocity profile for each t_0, and c) vertical velocity profile inverted for the shot #4.

Applying a logarithm function, the equation becomes linear in α. The attenuation tomography is computed after the P-wave velocity field so that the problem is reduced to a simple linear problem:

$$\alpha = \alpha + W^T \delta A \tag{15}$$

where α is the attenuation coefficient, δA the amplitude update and W the Fresnel weight matrix. Five iterations were performed starting from a simple homogeneous media with an attenuation $\alpha = 1.0\ e^{-03}$ Np.m^{-1} and the Fresnel weight matrix were calculated for the Q-N inverted Vp model at five frequencies (30 Hz, 45 Hz, 60 Hz, 90 Hz, and 120 Hz). Although the results are generally presented through the dimensionless quality factor, in our case, the dominant source frequency is almost constant for each shot (40 Hz) and the raw results are more contrasted. Moreover, because the definition of the quality factor can be different for highly attenuating materials (Schön, 1976), the attenuation map is imaged directly. A geomorphological inventory of the fissures was created from direct field observations in order to compare the attenuation map with a fissure map. All the fissures of width larger than 0.05 m were mapped. A Surface Cracking Index (SCI), defined as the total length of fissures per linear meter of the seismic profile, is calculated (Fig. 9a).

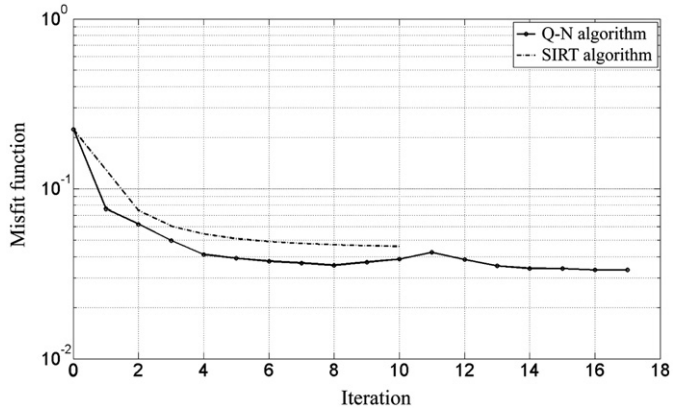

Fig. 7. Misfit function values for the Q-N and SIRT algorithms.

4. Interpretation and discussion

The seismic velocity model is first compared to the geometrical model of Travelletti and Malet (2012) constructed from the integration of multi-source data (e.g. electrical resistivity tomographies, dynamic penetration tests and geomorphological observations) at a coarser scale.

The bedrock depths obtained from penetration tests were used to deduce a minimum velocity of 850 m.s^{-1} corresponding to the limit between bedrock and the active layer, which position is then compared to the one of Travelletti and Malet (2012) along the profile (Fig. 10a, b). The thickness was calculated for both models with the surface topography observed in 2011. The observed depth interval is the same (from 2 to 13 m) and the global geometry of the bedrock is identical. The main differences are lower than 4 m and are located downhill of the profile, from the abscissa 100 to 230 m where the bedrock geometry is more complex. It shows important thickness variations that are less pronounced on the bedrock topography from Travelletti and Malet (2012).

To assess the quality of the Q-N algorithm result, the bedrock depth variation is compared to the topography visible on a black and white aerial orthophotograph of 1956 when the original relief was not covered by the landslide mass. Fig. 11a shows the orthophotograph of 1956 overlaid on a Digital Elevation Model (DEM) available for the same date. The seismic profile is also represented. A very irregular geometry of the relief composed of alternating crests and gullies of different sizes is observed. The studied profile crosses different geomorphic features. From point A to B (Fig. 11a), the topography seems first regular, before crossing a large thalweg. After crossing this thalweg, the profile reaches a long transversal crest that forms a bump and then plunges along the downhill slope. Those features are also observed in the P-wave tomogram, respectively at the abscissa 125, 140 and 160 m. Near the abscissa 180 m, a zone of low seismic velocities (<900 m.s^{-1}) is observed in depth that can be interpreted as a small gully, also visible as a black dot on the orthophotograph.

From these observations, an interpreted geological model that gathers geophysical and geomorphological information is proposed (Fig. 11b). The model is composed of three different materials. The first material, at depth, corresponds to the bedrock of Callovo–Oxfordian intact black marls characterized by seismic velocities greater than

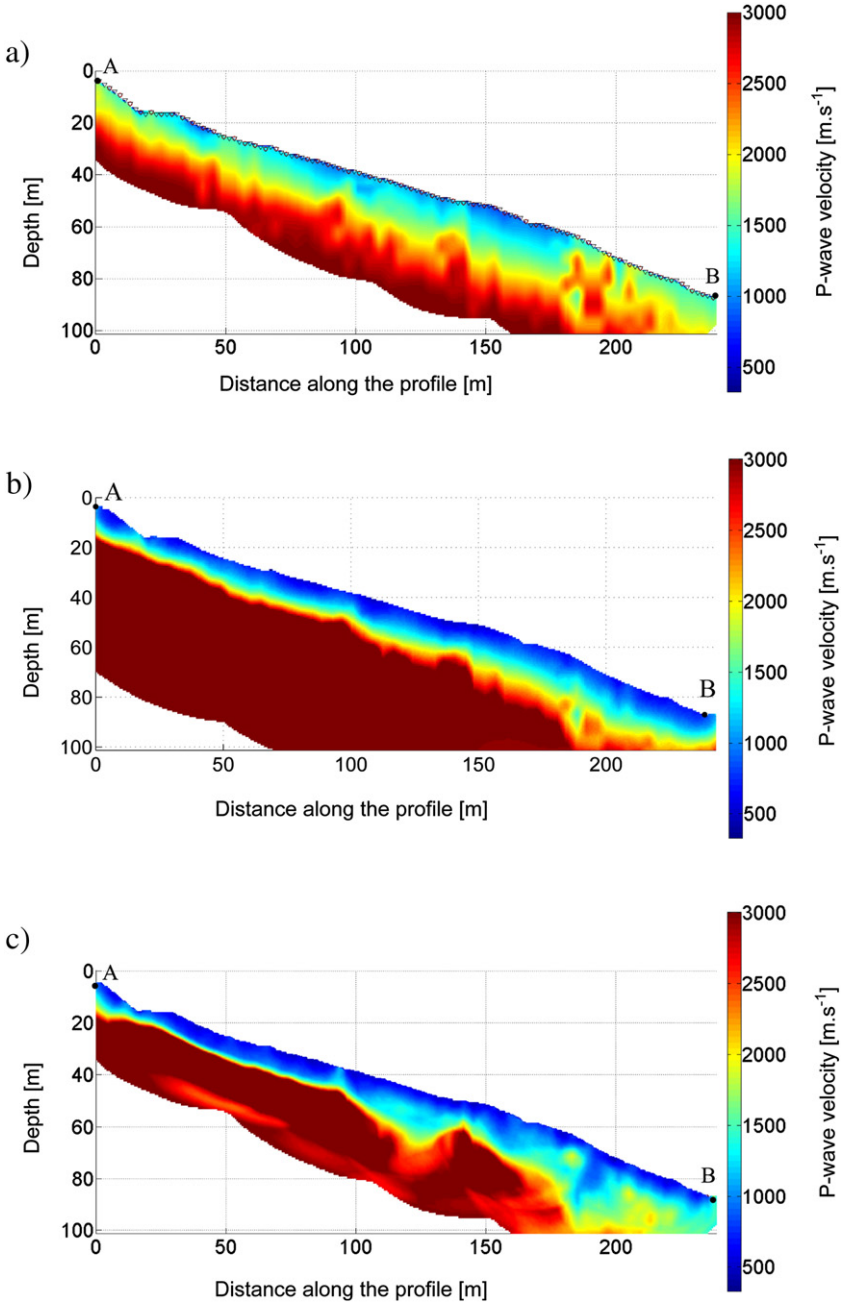

Fig. 8. Inversion results of the real dataset acquired on the Super-Sauze landslide: a) initial velocity model, b) inverted model with the SIRT algorithm of Grandjean and Sage (2004), and c) inverted model with the Q-N algorithm.

3000 $m.s^{-1}$ (Grandjean et al., 2007). The second material, characterized by a range of seismic velocities between 1500 and 2500 $m.s^{-1}$ is interpreted as a compacted landslide soil, because it is only present at a higher depth, where the height of soil above is sufficient to compact the landslide deposit. This layer, not involved in the dynamics of the landslide and quasi-impermeable, is called 'dead body' by several authors (Flageollet et al., 2000; Maquaire et al., 2001; Travelletti and Malet, 2012).

The third material corresponds to unconsolidated soils that present P-wave velocities between 400 and 1200 $m.s^{-1}$, characteristic of unconsolidated deposits (Bell, 2009). It constitutes the active unit of the landslide, i.e. the layer that concentrates the most deformation (Travelletti and Malet, 2012). To summarize, the Q-N algorithm permits to image correctly the structure of a clayey landslide with a better resolution than the SIRT algorithm (Grandjean and Sage, 2004) and gives the possibility to interpret the bedrock geometry with more details and a better resolution than previously. The seismic attenuation field is in agreement with the P-wave velocities. Although P-wave velocity and seismic attenuation are not linked during the inversion, the attenuation field also permits to distinguish the different materials. The first material, presenting a relatively low attenuation, corresponds to the bedrock and the "dead body". The attenuation values for this material are around 10^{-3} $Np.m^{-1}$, which are representative of consolidated soils at 40 Hz (Schön, 1976). The second material is more attenuating and heterogeneous, and corresponds to the upper unit of the landslide. The attenuation values for this unit vary from 4 to 12.10^{-3} $Np.m^{-1}$ which are typical values for unconsolidated soils at 40 Hz (Schön, 1976). The spatial lateral heterogeneity of the attenuation is important at the surface. Areas of high attenuation show attenuation values three times higher than others. The

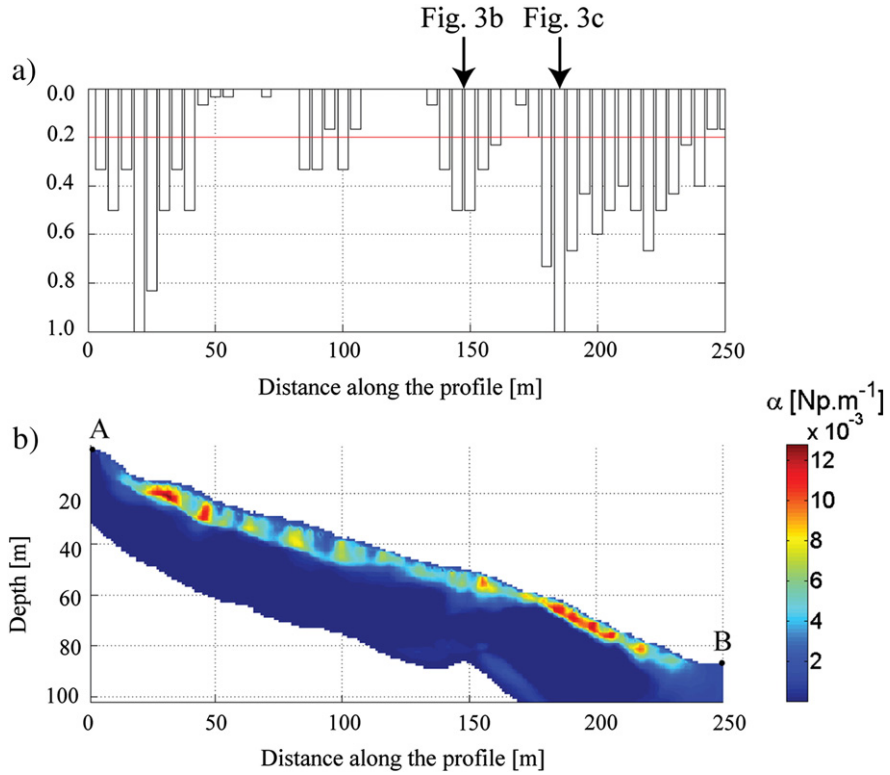

Fig. 9. Seismic wave attenuation tomography: a) Surface Cracking Index (SCI) and b) attenuation section inverted from the Super-Sauze data.

spatial correlation between the SCI and the attenuation is very good, so that we can confirm that attenuation variations are mainly caused by the various fissuring states observed at the surface. The seismic wave attenuation tomography highlights two important attenuation zones. The first one, in the upper-part at the abscissas 20–30 m seems to be concentrated at the interface between the landslide layer and the bedrock (Fig. 11b). In this area, the landslide material is affected by important shear stresses due to friction between the landslide layer and the bedrock topography (Stumpf et al., 2012). At the surface, fissures larger than 15 cm and measuring several meters in length are visible and the soil is completely remolded. The second zone seems to be associated to the influence of the local bedrock geometry that forms a bump followed by a steep slope downhill (Fig. 11b). Its concave shape is responsible of the tension fissures

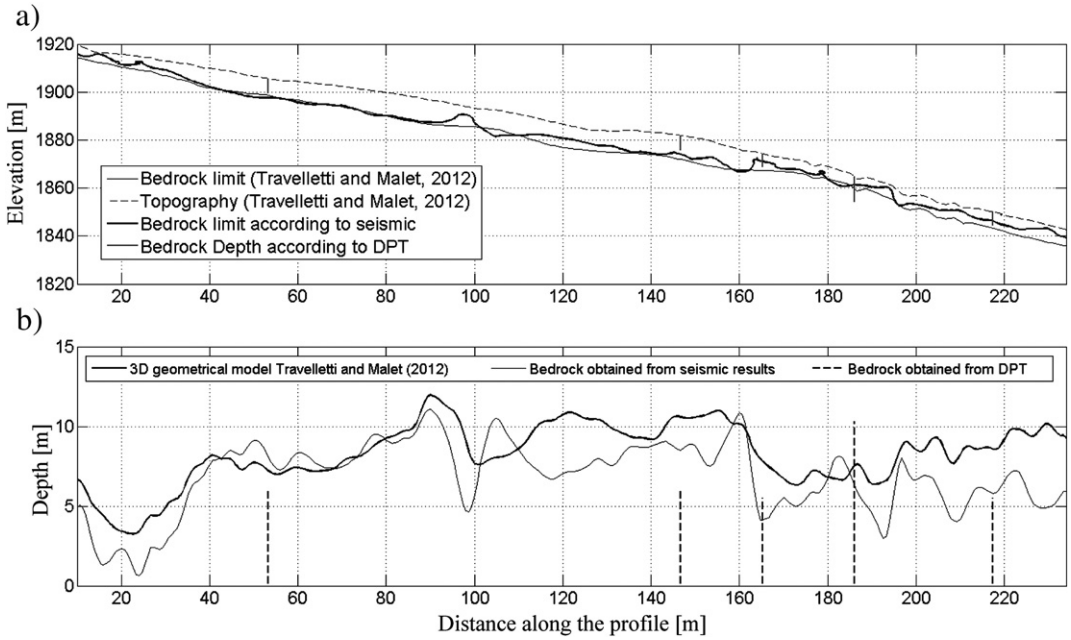

Fig. 10. Comparison of the bedrock geometry interpreted with the Q-N algorithm and with a geological modeler by integration of multi-source information at coarser spatial resolution (Travelletti and Malet, 2012) in terms of bedrock depth a) and layer thickness b).

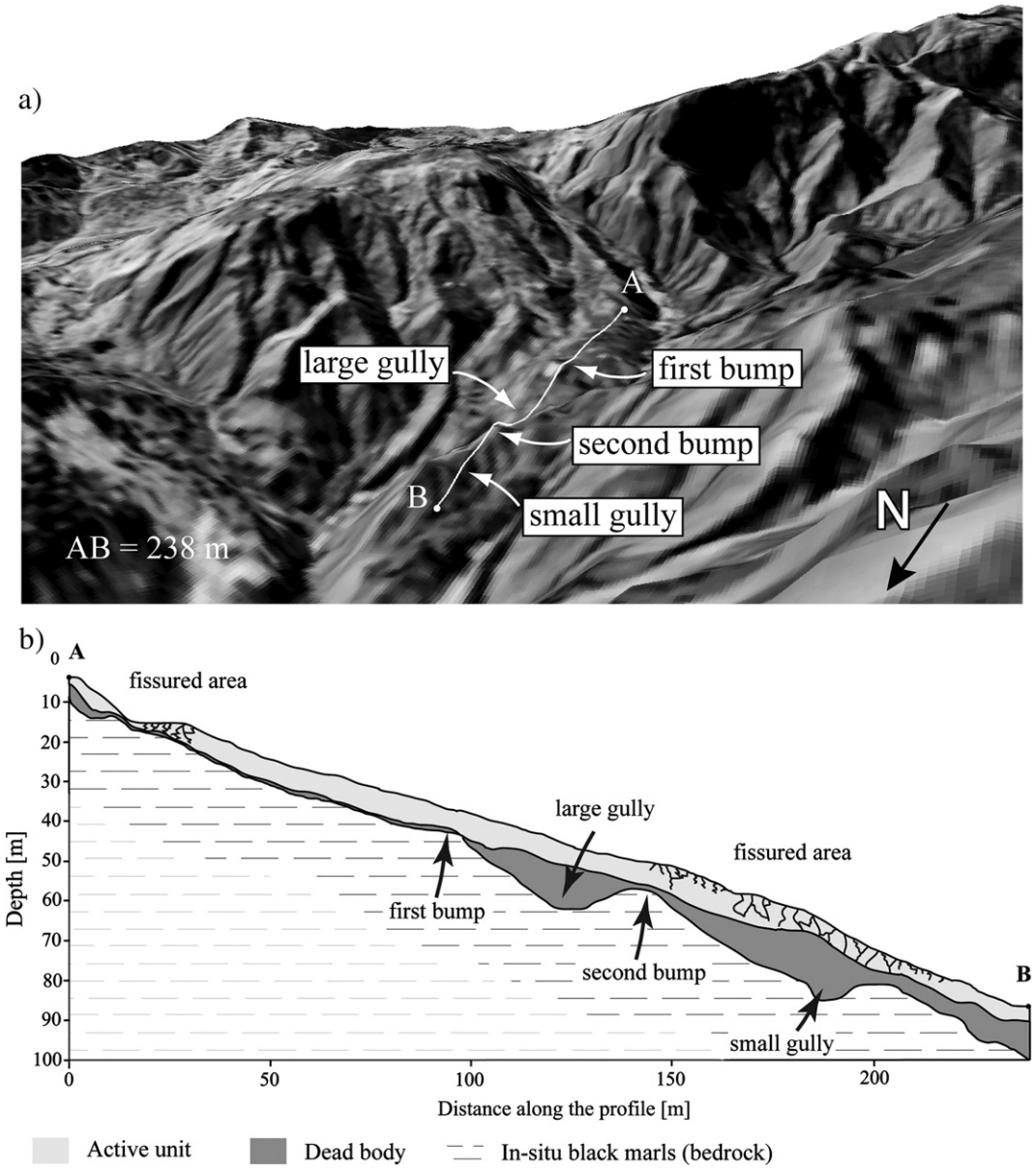

Fig. 11. a) Pre-event topography before the landslide and location of the seismic profile, b) interpreted geological cross-section in 3 layers: the active unit corresponds to the moving landslide layer, the dead body is a compacted and quasi-impermeable layer showing low displacements and the bedrock constituted of in-situ black marls.

well visible at the surface and clearly perpendicular to the major change of topography direction (Fig. 3c). Moreover, the soil is dryer in that zone because of the geometry of the area that facilitates the drainage of the groundwater table towards lower areas (Malet et al., 2005b).

The P-wave velocity and the seismic wave attenuation images are complementary. The P-wave velocity tomography is able to reproduce the sharp geometry of the bedrock and to differentiate the "dead body" from the bedrock (Fig. 11b). The seismic wave attenuation provides more information on the spatial lateral heterogeneity of the upper unit. However, the observed two high attenuation zones are not correlated with low values of P-wave velocity as a priori expected (Grandjean et al., 2011). This is explained by the seismic wavepaths going through this unconsolidated material that are probably too short to impact the velocity, so that only scattering and diffusion effects affect the wave amplitudes.

Finally, it is also important to note that this geophysical method is, in theory, not adapted to image the near surface zone (first meters in depth). Indeed, poor Fresnel weight coverage in that zone indicates that the final model is not very constrained. Moreover, the size of the fissures and of the attenuating objects in the landslide mass is certainly comparable to or even smaller than the size of the calculation cell (0.67 m).

5. Conclusions

A P-wave tomography inversion algorithm adapted to the characterization of highly heterogeneous media is presented. It combines an objective inversion regularization (based on the wave propagation principle) and takes into account the entire source frequency spectrum to improve the tomography resolution. The Fresnel wavepaths calculated for different source frequencies are used to retropropagate the traveltime residuals, assuming that in highly heterogeneous media, the first arrivals are only affected by velocity anomalies present in the first Fresnel zone. After verification of the ability of the algorithm to recover complex structures on a synthetic dataset, the method is applied on a real dataset

acquired at the Super-Sauze landslide. The results are in accordance with previous results from Travelletti and Malet (2012) and additional dynamic penetration tests. It appears that the sharp geometry of the bedrock topography is well recovered. This result is of first importance because bedrock geometry is one of the main controlling factors of the landslide dynamics. The attenuation field is then also inverted using the wavepaths calculated for P-wave velocity tomography. The dataset indicates that it is possible to use the amplitude of the first peak of the wave to get an accurate image of the seismic wave attenuation. The results are in agreement with the observed surface fissures inventory. The use of traveltimes and amplitude of waves permits to create an interpreted geological model that gathers those different details.

Acknowledgments

This work was supported by the French National Research Agency (ANR) within the Project SISCA "Système Intégré de Surveillance de Crises de glissements de terrains Argileux, 2009–2012" and the BRGM Carnot Institute.

References

Baina, R.M.H., 1998. Tomographie sismique entre puits: mise en œuvre et rôle de l'analyse à posteriori vers une prise en compte de la bande passante. Phd Thesis. Université Rennes 1, France.
Bell, F.G., 2009. Engineering Geology, Second edition. Elsevier, Oxford . 581p.
Bichler, A., Bobrowsky, P., Best, M., Douma, M., Hunter, J., Calvert, T., Burns, R., 2004. Three-dimensional mapping of a landslide using a multi-geophysical approach: the Quesnel Forks landslide. Landslides 1 (1), 29–40.
Bruno, F., Marillier, F., 2000. Test of high-resolution seismic reflection and other geophysical techniques on the Boup landslide in the Swiss Alps. Surveys in Geophysics 21, 333–348.
Ceverny, V., 2001. Seismic Ray Theory. Cambridge University Press, Cambridge. 713p.
Dahlen, F.A., 2005. Finite-frequency sensitivity kernels for boundary topography perturbations. Geophysical Journal International 162, 525–540.
Dahlen, F.A., Hung, S.H., Nolet, G., 2000. Fréchet kernels for finite-frequency traveltimes —I. Theory. Geophysical Journal International 141, 157–174.
De Castro Nunes, B.I., de Medeiros, W.E., do Nascimento, A.F., de Morais Moreira, J.A., 2011. Estimating quality factor from surface seismic data: a comparison of current approaches. Journal of Applied Geophysics 75, 161–170.
Debieche, T.-H., Marc, V., Emblanch, C., Cognard-Plancq, A.-L., Garel, E., Bogaard, T.A., Malet, J.-P., 2009. Local scale groundwater modelling in a landslide. The case of the Super-Sauze mudslide (Alpes-de-Haute-Provence, France). In: Malet, J.-P., Remaître, A., Boogard, T.A. (Eds.), Proceedings of the International Conference on Landslide Processes: From Geomorphologic Mapping to Dynamic Modeling. CERG Editions, Strasbourg, pp. 101–106.
Flageollet, J.-C., Malet, J.-P., Maquaire, O., 2000. The 3D structure of the Super-Sauze earthflow: a first stage towards modelling its behavior. Physics and Chemistry of the Earth 25, 785–791.
Glade, T., Stark, P., Dikau, R., 2005. Determination of potential landslide shear plane depth using seismic refraction. A case study in Rheinhessen, Germany. Bulletin of Engineering Geology and the Environment 64, 151–158.
Grandjean, G., Sage, S., 2004. JaTS: a fully portable seismic tomography software based on Fresnel wavepaths and a probabilistic reconstruction approach. Computers and Geosciences 30, 925–935.
Grandjean, G., Pennetier, C., Bitri, A., Meric, O., Malet, J.-P., 2006. Caractérisation de la structure interne et de l'état hydrique de glissements argilo-marneux par tomographie géophysique: l'exemple du glissement-coulée de Super-Sauze (Alpes du Sud, France). Comptes Rendus Geosciences 338, 587–595.
Grandjean, G., Malet, J.-P., Bitri, A., Méric, O., 2007. Geophysical data fusion by fuzzy logic for imaging the mechanical behaviour of mudslides. Bulletin de la Société Géologique de France 177 (2), 127–136.
Grandjean, G., Gourry, J.-C., Sanchez, O., Bitri, A., Garambois, S., 2011. Structural study of the Ballandaz landslide (French Alps) using geophysical imagery. Journal of Applied Geophysics 75, 531–542.
Grandjean, G., Bitri, A., Krzeminska, M., 2012. Characterization of a landslide fissure pattern by integrating seismic azimuth tomography and geotechnical testing. Hydrological Processes 26 (14), 2120–2127.
Hagedoorn, J.G., 1959. The plus–minus method of interpreting seismic refraction sections. Geophysical Prospecting 7 (2), 158–182.
Jongmans, D., Garambois, S., 2007. Geophysical investigation of landslides: a review. Bulletin de la Société Géologique de France 178 (2), 101–112.
Kissling, E., Husen, S., Haslinger, F., 2001. Model parameterization in seismic tomography: a choice of consequence for the solution quality. Physics of the Earth and Planetary Interiors 123, 89–101.
Liu, Y., Dong, L., Wang, Y., Zhu, J., Ma, Z., 2009. Sensitivity kernels for seismic Fresnel volume tomography. Geophysics 74, U35–U46.
Malet, J.-P., Auzet, A.-V., Maquaire, O., Ambroise, B., Descroix, L., Estèves, M., Vandervaere, J.-P., Truchet, E., 2003. Soil surface characteristics influence on infiltration in black marls: application to the Super-Sauze earthflow (Southern Alps, France). Earth Surface Processes and Landforms 28, 547–564.
Malet, J.-P., Laigle, D., Remaître, A., Maquaire, O., 2005a. Triggering conditions and mobility of debris-flows associated to complex earthflows. Geomorphology 66 (1–4), 215–235.
Malet, J.-P., van Asch, Th.W.J., Van Beek, L.P.H., Maquaire, O., 2005b. Forecasting the behaviour of complex landslides with a spatially distributed hydrological model. Natural Hazards and Earth System Sciences 5, 71–85.
Maquaire, O., Flageollet, J.C., Malet, J.-P., Schmutz, M., Weber, D., Klotz, S., Albouy, Y., Descloîtres, M., Dietrich, M., Guérin, R., 2001. Une approche multidisciplinaire pour la connaissance d'un glissement-coulée dans les marnes noires du Callovien-Oxfordien:(Super-Sauze, Alpes-de-Haute-Provence, France). Revue française de géotechnique 95–96, 15–31.
Maquaire, O., Malet, J.-P., Remaître, A., Locat, J., Klotz, S., Guillon, J., 2003. Instability conditions of marly hillslopes: towards landsliding of gullying? The case of the Barcelonnette Basin, South East France. Engineering Geology 70, 109-130.
Mauritsch, H.J., Seiberl, W., Arndt, R., Römer, A., Schneiderbauer, K., Sendlhofer, G.P., 2000. Geophysical investigations of large landslides in the Carnic Region of southern Austria. Engineering Geology 56, 373–388.
Méric, O., 2006. Etude des mouvements de terrain par méthodes géophysiques. Phd Thesis. Université Joseph Fourier, 252p.
Nolet, G., 1985. Solving or resolving inadequate and noisy tomographic systems. Journal of Computational Physics 61, 463–482.
Nolet, G., 1987. Seismic wave propagation and seismic tomography. In: Nolet, G. (Ed.), Seismic Tomography. Reidel, Dordrecht, pp. 1–23.
Paige, C., Saunders, M., 1982. LSQR: an algorithm for sparse linear equations and sparse least squares. ACM Transaction on Mathematical Software 8, 43–71.
Palmer, D., Burke-Kenneth, B.S., 1980. The Generalized Reciprocal Method of Seismic Refraction Interpretation. Society of Exploration Geophysicists, Tulsa . 104 p.
Podvin, P., Lecompte, I., 1991. Finite difference computation of traveltimes in very contrasted velocity model: a massively parallel approach and its associated tools. Geophysical Journal International 105, 271–284.
Popovici, M., Sethian, J., 1998. Three dimensional traveltimes using the fast marching method. In: Hassanzadeh, S. (Ed.), Proceedings SPIE 3453, Mathematical Methods in Geophysical Imaging V. 82p.
Pratt, R.G., 1999. Seismic waveform inversion in the frequency domain. Part 1: theory and verification in a physic scale model. Geophysics 64, 888–901.
Romdhane, A., Grandjean, G., Brossier, R.M., Réjiba, F., Operto, S., Virieux, J., 2011. Shallow-structure characterization by 2D elastic full-waveform inversion. Geophysics 76, 81–93.
Samyn, K., Travelletti, J., Bitri, A., Grandjean, G., Malet, J.-P., 2012. Characterization of a landslide geometry using 3D seismic refraction traveltime tomography: the La Valette landslide case history. Journal of Applied Geophysics 86, 120–132.
Schmutz, M., Albouy, Y., Guérin, R., Maquaire, O., Vassal, J., Schott, J.-J., Descloîtres, M., 2000. Joint electrical and time domain electromagnetism (TDEM) data inversion applied to the Super-Sauze earthflow (France). Surveys in Geophysics 21, 371–390.
Schön, J.H., 1976. The Physical Properties of Rocks: Fundamentals and Principles of Petrophysics. Pergamon, New York . 601p.
Schrott, L., Sass, O., 2008. Application of field geophysics in geomorphology: advances and limitations exemplified by case studies. Geomorphology 93, 55–73.
Sirgue, L., Pratt, R.G., 2004. Efficient waveform inversion and imaging: a strategy for selecting temporal frequencies. Geophysics 69, 231–248.
Spetzler, J., Snieder, R., 2004. The Fresnel volume and transmitted waves. Geophysics 69, 653–663.
Spetzler, J., Xue, Z., Saito, H., Nishizawa, O., 2008. Case story: timelapse seismic crosswell monitoring of CO_2 injected in an onshore sandstone aquifer. Geophysical Journal International 172, 214–225.
Stumpf, A., Malet, J.-P., Kerle, N., Niethammer, U., Rothmund, S., 2012. Image-based mapping of surface fissures for the investigation of landslide dynamics. Geomorphology 24p.
Sun, J., Sun, Z., Han, F., 2011. A finite difference scheme for solving the eikonal equation including surface topography. Geophysics 76, T53.
Tarantola, A., 1987. Inverse problem theory. Methods for Data Fitting and Model Parameters Estimation. Society of Industrial and Applied Mathematics, Philadelphia . 342p.
Taillandier, C., Noble, M., Chauris, H., Calandra, H., 2009. First arrival traveltime tomography based on the adjoint-state method. Geophysics 74 (6), WCB1–WCB10.
Trampert, J., Lévèque, J.-J., 1990. Simultaneous iterative reconstruction technique: physical interpretation based on the generalized least squares solution. Journal of Geophysical Research 95, 553–559.
Travelletti, J., Malet, J.-P., 2012. Characterization of the 3D geometry of flow-like landslides: a methodology based on the integration of heterogeneous multi-source data. Engineering Geology 128, 30–48.
Travelletti, J., Malet, J.-P., Samyn, K., Grandjean, G., Jaboyedoff, M., in press. Control of landslide retrogression by discontinuities: evidences by the integration of airborne- and ground-based geophysical information. Landslides. http://dx.doi.org/10.1007/s10346-011-0310-8.
van Asch, Th.W.J., Malet, J.-P., van Beek, L.H.P., 2006. Influence of landslide geometry and kinematic information to describe the liquefaction of landslides: some theoretical considerations. Engineering Geology 88, 59–69.
van Dam, R.L., 2010. Landform characterization using geophysics—recent advances, applications, and emerging tools. Geomorphology 137 (1), 57–73.
van der Sluis, A., van der Vorst, H.A., 1987. Numerical solutions of large, sparse linear systems arising from tomographic problems. In: Nolet, G. (Ed.), Seismic Tomography with Applications in Global Seismology and Exploration Geophysics. Reidel, Dordrecht, pp. 53–87.
Vasco, D.W., Peterson, J.E., Majer, E.L., 1995. Beyond ray tomography: wavepaths and Fresnel volumes. Geophysics 60, 1790–1804.
Vidale, J., 1988. Finite-difference calculation of travel time. Bulletin of the Seismological Society of America 78, 2062–2076.

Virieux, J., Operto, S., 2009. An overview of full waveform inversion in exploration geophysics. Geophysics 74 (6), WCC1–WCC26.
Watanabe, T., Sassa, K., 1996. Seismic attenuation tomography and its application to rock mass evaluation. International Journal of Rock Mechanics and Mining Sciences 33 (5), 467–477.
Watanabe, T., Matsuoka, T., Ashida, Y., 1999. Seismic traveltime tomography using Fresnel volume approach. 69th Proceedings, Society Exploration Geophysics, Houston, USA, SPRO12.5.
Yomogida, K., 1992. Fresnel zone inversion for lateral heterogeneities in the Earth. Pure and Applied Geophysics 138, 391–406.
Zelt, C.A., Barton, P.J., 1998. Three-dimensional seismic refraction tomography: a comparison of two methods applied to data from the Faeroe Basin. Journal of Geophysical Research 103 (B4), 7187–7210.
Zhao, H., 2005. A fast sweeping method for eikonal equations. Mathematics of Computation 74, 603–627.
Zhao, L., Jordan, T.H., 2006. Structural sensitivities of finite-frequency seismic waves: a full-wave approach. Geophysical Journal International 165, 981–990.